Monthly Notices of the ROYAL ASTRONOMICAL SOCIETY

MNRAS **511,** 2814–2828 (2022) https://doi.org/10.1093/mnras/stac230
Advance Access publication 2022 January 31

Grids of stellar models with rotation VII: models from 0.8 to 300 $M_\odot$ at supersolar metallicity ($Z = 0.020$)

Norhasliza Yusof [1]★ Raphael Hirschi,[2,3] Patrick Eggenberger,[4] Sylvia Ekström [4] Cyril Georgy,[4] Yves Sibony [4] Paul A. Crowther,[5] Georges Meynet,[4] Hasan Abu Kassim,[1] Wan Aishah Wan Harun,[1] André Maeder,[4] Jose H. Groh,[6] Eoin Farrell [6] and Laura Murphy[6]

[1]*Department of Physics, Faculty of Science, University of Malaya, 50603 Kuala Lumpur, Malaysia*
[2]*Astrophysics Group, Keele University, Keele, Staffordshire ST5 5BG, UK*
[3]*Institute for Physics and Mathematics of the Universe (WPI), University of Tokyo, 5-1-5 Kashiwanoha, Kashiwa 277-8583, Japan*
[4]*Department of Astronomy, University of Geneva, Chemin Pegasi 51, CH-1290 Versoix, Switzerland*
[5]*Department of Physics & Astronomy, University of Sheffield, Hounsfield Road, Sheffield S3 7RH, UK*
[6]*School of Physics, Trinity College Dublin, The University of Dublin, College Green, Dublin 2, Ireland*

Accepted 2022 January 20. Received 2022 January 19; in original form 2021 November 22

ABSTRACT

We present a grid of stellar models at supersolar metallicity ($Z = 0.020$) extending the previous grids of Geneva models at solar and sub-solar metallicities. A metallicity of $Z = 0.020$ was chosen to match that of the inner Galactic disc. A modest increase of 43 per cent (= 0.02/0.014) in metallicity compared to solar models means that the models evolve similarly to solar models but with slightly larger mass-loss. Mass-loss limits the final total masses of the supersolar models to 35 $M_\odot$ even for stars with initial masses much larger than 100 $M_\odot$. Mass-loss is strong enough in stars above 20 $M_\odot$ for rotating stars (25 $M_\odot$ for non-rotating stars) to remove the entire hydrogen-rich envelope. Our models thus predict SNII below 20 $M_\odot$ for rotating stars (25 $M_\odot$ for non-rotating stars) and SNIb (possibly SNIc) above that. We computed both isochrones and synthetic clusters to compare our supersolar models to the Westerlund 1 (Wd1) massive young cluster. A synthetic cluster combining rotating and non-rotating models with an age spread between $\log_{10}$(age/yr) = 6.7 and 7.0 is able to reproduce qualitatively the observed populations of WR, RSG, and YSG stars in Wd1, in particular their simultaneous presence at $\log_{10}(L/L_\odot) = 5$–5.5. The quantitative agreement is imperfect and we discuss the likely causes: synthetic cluster parameters, binary interactions, mass-loss and their related uncertainties. In particular, mass-loss in the cool part of the HRD plays a key role.

Key words: stars: evolution – stars: massive – stars: rotation.

1 INTRODUCTION

Large homogeneous grids of stellar models facilitate the analysis and interpretation of a wide range of observations. They also enable us to study the dependence of stellar evolution on key parameters like mass, metallicity, and rotation. There are several large published grids of evolutionary models covering various mass and metallicity ranges and including various input physics. Examples include the grid from Spada et al. (2017) focused on low-mass stars with solar-scaled composition and the grids of evolutionary models for rotating main-sequence stars with initial composition tailored to the Galaxy and Magellanic Clouds and including transport by magnetic fields (Brott et al. 2011). The PARSEC data base (Bressan et al. 2012; Chen et al. 2015) covers a broad range of metallicities ($0.0001 \leq Z \leq 0.04$) and initial masses up to 350 $M_\odot$. This data base adopted solar abundances from Caffau et al. (2011). The MIST data base (Choi et al. 2016; Dotter 2016) adopted solar-scaled abundances from Asplund et al. (2009) with a mass range from 0.1 to 300 $M_\odot$ and metallicities within ($-4.0 \leq$ [Z/H] ≤ 0.5). Finally, the BaSTI data base (Pietrinferni et al. 2004, 2006; Hidalgo et al. 2018) includes a solar-scaled composition grid with initial composition ranging from [Fe/H] = −3.20 to +0.45 and initial masses up to 15 $M_\odot$ and a grid with α-enhanced heavy element distribution (Pietrinferni et al. 2021).

Grids of single star models with and without rotation at $Z = 0.014$, 0.006, 0.002, 0.0004, 0.0, thus covering a wide range of metallicities from solar to primordial stars via the metallicities of the LMC, SMC, and I Zw 18 (Ekström et al. 2012; Georgy et al. 2013; Groh et al. 2019; Eggenberger et al. 2021; Murphy et al. 2021) have been completed using the Geneva Stellar Evolution Code (GENEC; see Eggenberger et al. 2008, for details). This paper extends the GENEVA grids of models to supersolar metallicity. The grid of models starting with Ekström et al. (2012) is a major update of the previous generation of GENEVA grids published in the 1990s (e.g. Schaller et al. 1992; Meynet et al. 1994) and Ekström et al. (2012) describe the updates in input physics between the two grids. Two major updates are first the inclusion of rotation in the models and second an update of the solar composition following the work of Asplund (2005). The reference solar metallicity used in the present grid is $Z = 0.014$ (versus $Z = 0.02$ used in Schaller et al. 1992). A metallicity of $Z = 0.02$ for this supersolar metallicity grid was chosen to match that of the inner Milky Way, including the Galactic Centre itself.

★ E-mail: norhaslizay@um.edu.my

There is a well-established metallicity gradient in the Galactic disc, with slope –0.03 to –0.07 dex kpc^{-1} (Balser et al. 2011), such that the representative metallicity at the end of the Galactic Bar will be ∼0.15 dex or 40 per cent higher than in the Solar neighbourhood (Asplund, Amarsi & Grevesse 2021, log O/H + 12 = 8.69), although there is some evidence for azimuthal variations (Davies et al. 2009). Although the Galactic Centre region has been observed for a long time, improvements in instrumentation have led to large numbers of massive stars available for quantitative study (Liermann, Hamann & Oskinova 2009; Clark et al. 2018a). While stellar evolution properties could be extrapolated from solar metallicity models, it is preferable to provide stellar models tailored to the higher metallicity of the inner Galaxy, which is the goal of this paper.

While some published grids of models also use a metallicity $Z = 0.02$ (e.g. Schaller et al. 1992; Eldridge & Vink 2006; Stanway & Eldridge 2018), the present grid of models is supersolar so should not be compared to the $Z = 0.02$ models that consider $Z = 0.02$ as their solar metallicity (e.g. Schaller et al. 1992; Stanway & Eldridge 2018). Instead, they can be compared to published supersolar models (e.g. the $Z = 0.04$ of Meynet et al. 1994). The main reason for this is that mass-loss is scaled using the ratio of the metallicity of the models relative to the reference solar composition considered. In this context, the present grid of model corresponds to [Fe/H] = 0.155 (or a factor of 1.429 = 0.02/0.014). This being said, given the many changes in input physics between this and published grids of supersolar models (e.g. Meynet et al. 1994) and the fact that most supersolar grids of models use a value of Z that is twice the solar value (versus only 1.429 in this grid), such comparisons offer limited insight. The grid of supersolar rotating models closest to the present grid is the [Fe/H] = 0.25 grid of the MIST data base (Choi et al. 2016; Dotter 2016) and we compare the present models to the MIST grid in Section 4.

The present grid of models is tailored for the inner Galactic disc, which contains several massive young star clusters. The best studied massive young star cluster in the inner Galactic disc is Westerlund 1 (Wd1), at a distance of ∼4 kpc (Beasor et al. 2021), while there are also several older massive clusters at the end of the Galactic Bar which are rich in red supergiants (Davies et al. 2009). Within the Galactic Centre, at a distance of 8.2 kpc (GM SHOULD BE PC NOT KPC; Gravity Collaboration 2019), there are several young high-mass ($\geq 10^4$ M$_\odot$) clusters including the Arches, Quintuplet, and Galactic Centre clusters, plus a rich massive star population within the Central Molecular Zone (Clark et al. 2021). We compare the present models to these clusters in Section 4.

The models presented in this paper will also be useful for extra-galactic studies of metal-rich (massive) galaxies undergoing high star formation rates (SFR). Within the Local Group, the present-day metallicity of M31 is considered to be highly supersolar based on strong-line H II region calibrations (Zaritsky, Kennicutt & Huchra 1994), such that $Z = 0.03$ is commonly adopted. However, more recent direct H II determinations infer a central metallicity of log O/H + 12 = 8.7 to 8.9 (Zurita & Bresolin 2012), with similar abundances from early-type stars in the inner disc (Venn et al. 2000; Smartt et al. 2001), such that $Z = 0.02$ is more suitable to M31. Stellar abundances as high as log O/H +12 = 9.0 have been obtained (Trundle et al. 2002), potentially attributable to azimuthal variations. Beyond the Local Group, there are known to be many high metallicity star-forming regions (Bresolin et al. 2005) the most metal-rich being log O/H + 12 = 8.9, 60 per cent higher than the Sun, according to standard nebular diagnostics. Bresolin et al. (2016) have highlighted still higher stellar abundances of log O/H + 12 = 9.0 close to the centre of M83, with both stellar and nebular diagnostics favouring slightly supersolar abundances within the inner disc.

Table 1. Initial composition of the models. The number in bracket is the exponent: e.g. 4.540 (−5) = 4.540 × 10^{-5}.

Nuclide	Initial mass fraction	Nuclide	Initial mass fraction
^{1}H	7.064 (−1)	^{17}O	3.237 (−6)
^{3}He	4.540 (−5)	^{18}O	1.843 (−5)
^{4}He	2.735 (−1)	^{20}Ne	2.681 (−3)
^{12}C	3.261 (−3)	^{22}Ne	2.169 (−4)
^{13}C	3.958 (−5)	^{24}Mg	7.193 (−4)
^{14}N	9.411 (−4)	^{25}Mg	9.488 (−5)
^{15}N	3.707 (−6)	^{26}Mg	1.086 (−4)
^{16}O	8.169 (−3)		

This paper is structured as follows. A summary of physical ingredients is provided in Section 2, results are presented in Section 3, comparisons with observations are provided in Section 4 with a discussion and conclusions drawn in Section 5.

2 PHYSICAL INGREDIENTS OF THE MODELS

The physical ingredients of the present grid of models are the same as in the other papers in the series for consistency. These are described in detail in Ekström et al. (2012) (solar grid hereinafter) and we only summarize them here.

The initial composition of the models is given in Table 1. In particular, the initial abundances of H, He, and metals are set to X = 0.7064, Y = 0.2735, and Z = 0.02. The mixture of heavy elements is solar-scaled (scaled from $Z = 0.014$ to $Z = 0.02$ compared to Ekström et al. 2012) with the solar mixture based on Asplund, Grevesse & Sauval (2005) except for the Ne abundance, which is based on the work by Cunha, Hubeny & Lanz (2006). Using this scaling, [Fe/H] = 0.155. Isotopic ratios are taken from Lodders (2003).

The Schwarzschild criterion is used to determine the location of convective boundaries. Convective boundary mixing (CBM) is only applied to hydrogen and helium burning cores in the form of overshooting with an overshooting distance $l_{ov} = 0.1\,H_P$ for $M \geq 1.7$ M$_\odot$, 0.05 H_P between 1.25 and 1.5 M$_\odot$, and 0 below (where H_P is the pressure scale-height scale at the Schwarzschild convective boundary). Studies such as Castro et al. (2014) observe a wider main sequence (MS) width for massive stars than predicted by models using $l_{ov} = 0.1\,H_P$. Models using a larger value of overshoot (e.g. 0.035 in Brott et al. 2011) predict a larger MS that fits the MS width inferred for 15 M$_\odot$ stars by Castro et al. (2014) but still fail to explain the mass dependence of the MS width. The uncertainties linked to CBM and their impact on the evolution of massive stars have been studied extensively (see e.g. Vink et al. 2010; Davis, Jones & Herwig 2019; Higgins & Vink 2019; Kaiser et al. 2020; Martinet et al. 2021; Scott et al. 2021). These studies generally find that using larger CBM (such as overshoot) leads to larger convective cores, higher luminosities and models behaving like more massive models with less CBM. Using larger CBM would for example tend to decrease the minimum mass for a single star to become a Wolf–Rayet (WR) star. We nevertheless continue using $l_{ov} = 0.1\,H_P$ in this supersolar grid of models for consistency with the grids at other metallicities.

The stellar equations are modified to include the effects of rotation using the shellular-rotation hypothesis. The main rotation-induced instabilities included in the models are meridional circulation and (secular and dynamical) shear. For the transport of angular momentum, meridional circulation is implemented as an advective process during the MS phase while shear is implemented as a

diffusive process.[1] Both processes are implemented in a diffusive approach for the transport of chemical elements (see Ekström et al. 2012, for more details and references). Magnetic instabilities are not included in the grids of models.

The recipes for mass-loss rates ($\dot{M}$) used depend on mass, surface composition, and position in the Hertzsprung–Russell (HR) diagram, and for consistency we follow the approach of previous grids. On the MS, stars with a mass below 7 $M_\odot$ are computed at constant mass. Above 7 $M_\odot$, the radiative mass-loss rate adopted is from Vink, de Koter & Lamers (2001). In the domains not covered by this prescription, the prescription from de Jager, Nieuwenhuijzen & van der Hucht (1988) is used. For red (super)giants (RG/RSG), the Reimers (1975, 1977) formula (with $\eta = 0.5$) is used for stars up to 12 $M_\odot$. The de Jager et al. (1988) prescription is applied from 15 $M_\odot$ and above for models with $\log(T_{\rm eff}) > 3.7$. For $\log(T_{\rm eff}) \leq 3.7$, a linear fit of the data from Sylvester, Skinner & Barlow (1998) and van Loon et al. (1999) (see Crowther 2000) is used. Massive star models in the RSG phase sometimes have layers that exceed the Eddington luminosity limit. There are no theoretical prescriptions for mass-loss in the RSG phase, and no precise observational or theoretical guidance for cases when the Eddington luminosity is exceeded. In order to nevertheless take into account when models exceed the Eddington limit, mass-loss rates are increased by a factor of 3 whenever the luminosity of any of the layers of the envelope is higher than 5 times the Eddington luminosity (see Ekström et al. 2012, for more details and a discussion on this topic). WR stars are computed with the Nugis & Lamers (2000) prescription, or the Gräfener & Hamann (2008) recipe in the small validity domain of this prescription. In some cases, the WR mass-loss rate from Gräfener & Hamann (2008) is lower than the rate from Vink et al. (2001). In these cases, the Vink et al. (2001) prescription is used instead. Both the Nugis & Lamers (2000) and Gräfener & Hamann (2008) mass-loss rates account for some clumping effects (Muijres et al. 2011) and are a factor of 2 to 3 smaller than the 'normal' rates used in the 1992 grids (Schaller et al. 1992).

For rotating models, a correction factor is applied to the radiative mass-loss rate as described in Maeder & Meynet (2000):

$$\dot{M}(\Omega) = F_\Omega \cdot \dot{M}(\Omega = 0) = F_\Omega \cdot \dot{M}_{\rm rad} \quad \text{with} \quad F_\Omega = \frac{(1-\Gamma)^{\frac{1}{\alpha}-1}}{\left[1 - \frac{\Omega^2}{2\pi G \rho_{\rm m}} - \Gamma\right]^{\frac{1}{\alpha}-1}}, \tag{1}$$

where $\Gamma = L/L_{\rm Edd} = \kappa L/(4\pi cGM)$ is the Eddington factor (with κ is the electron-scattering opacity), Ω is the angular velocity, and α is the force multiplier parameter depending on $T_{\rm eff}$.

Historically, empirical mass-loss rates were derived using a mixture of rotating and non-rotating stars. To compensate for this fact, $\dot{M}(\Omega = 0)$ is set to 0.85 times the mass-loss rate obtained from the prescriptions above during the MS (main phase during which rotation rates are significant). This reduction factor does not need to be applied to the theoretical mass-loss rate of Vink et al. (2001) but the 0.85 factor was still used in this grid of models for historical reasons and consistency with the grids at other metallicities. For the same historical reasons some MESA models (Farmer et al. 2016; Ritter et al. 2018) apply a factor of 0.8 to mass-loss prescriptions. We no longer recommend to use such reduction factor, especially for theoretical mass-loss prescriptions such as Vink et al. (2001) or phases during which the average rotation rate is small (e.g. RSG phase).

The impact of the 0.85 reduction factor applied during the MS and in general of the mass-loss enhancement factor due to rotation (F_Ω) remains very modest in the present grid of models and do not affect our conclusions. Indeed, the rotating 20 and 25 $M_\odot$ models lose 2.88 and 0.63 $M_\odot$, respectively, (see Table A1) during the MS when these factors would modify the mass-loss rate. This is much smaller than the mass-loss in the RSG phase (more than 10 $M_\odot$ for both models), during which rotation is very slow and the mass-loss rate applied are not modified by equation (1). So most of the mass-loss in the 20–25 $M_\odot$ mass range is lost during RSG phase where rotating rates are low and the key factor determining mass-loss is the luminosity. The other effects of rotation, rotation-induced mixing in particular, have a much larger impact on mass-loss than the enhancement factors above by helping models in this mass range to reach the RSG early. For higher initial masses, $M \gtrsim 40\,M_\odot$, mass-loss during the MS becomes significant (half of the initial mass or more for $M \gtrsim 85\,M_\odot$) so the enhancement factor above may play a role, especially if the model is close to the Eddington limit. In the present grid of models, however, mass-loss is strong in both rotating and non-rotating model, keeping the very massive models away from the Eddington limit and the dominant impact of rotation is its indirect effects on the effective temperature and luminosity of the models.

Mass-loss rates are scaled with metallicity in the following way: $\dot{M}(Z) = (Z/Z_\odot)^\alpha \dot{M}(Z_\odot)$. For the MS and blue supergiant phases, we assume $\alpha = 0.85$ or 0.50 when the Vink et al. (2001) or de Jager et al. (1988) recipes are used, respectively. For the WR phase, we assume $\alpha = 0.66$, following Eldridge & Vink (2006). For other phases, such as when the effective temperature $T_{\rm eff}$ is lower than $\log(T_{\rm eff}/K = 3.7)$, no metallicity scaling is applied. Given the ratio of 0.02/0.014 = 1.43, mass-loss rates are larger by a factor between 1 ($\log_{10}(T_{\rm eff}/K) < 3.7$) and 1.35 ($\alpha = 0.85$) in a supersolar model compared to the corresponding solar metallicity model.

3 PROPERTIES OF THE STELLAR MODELS

We computed stellar evolution models for the following initial masses: 0.8, 0.9, 1, 1.1, 1.25, 1.35, 1.5, 1.7, 2, 2.5, 3, 4, 5, 7, 9, 12, 15, 20, 25, 32, 40, 60, 85, 120, 150, 200, and 300 $M_\odot$. For each mass, we computed both a non-rotating and a rotating model with a ratio between the equatorial surface rotational velocity ($V_{\rm ini}$) and critical rotational velocity ($V_{\rm crit}$) of 0.4 (0 for the non-rotating models) at the zero-age main sequence (ZAMS). The models are evolved up to the end of core carbon burning ($M_{\rm ini} \geq 12\,M_\odot$), the early asymptotic giant branch ($2.5\,M_\odot \leq M_{\rm ini} \leq 9\,M_\odot$), or the helium flash ($M_{\rm ini} \leq 2\,M_\odot$).

The main properties of the models at key stages (ZAMS, TAMS, and end of He- and C-burning phases if relevant) are presented in Tables 2 and A1. Similarly to Ekström et al. (2012) and Georgy et al. (2013), electronic tables of the evolutionary sequences are publicly available.[2] For each model, the evolutionary track is described by 400 selected data points, with each one corresponding to a given evolutionary stage. Points of different evolutionary tracks with the same number correspond to similar stages to facilitate the interpolation of evolutionary tracks. The points are numbered as described in Ekström et al. (2012). The grids can thus be used as input for computing interpolated tracks, isochrones, and population synthesis models

[1] After the MS phase, in the present models, the main effect impacting the internal rotation is the local conservation of the angular momentum.

[2] See http://obswww.unige.ch/Recherche/evol/-Database- or the CDS data base at http://vizier.u-strasbg.fr/viz-bin/VizieR-2.

Table 2. Initial mass ($M_{\rm ini}$) and ratio of the initial equatorial surface velocity ($V_{\rm ini}/V_{\rm crit}$) followed by the final total ($M_{\rm fin}$), helium-core ($M_{\alpha,01}$ defined as the mass coordinate where the hydrogen mass fraction drops below 1 per cent) and carbon-oxygen core masses ($M_{\rm CO,01}$ defined as the mass coordinate where the helium mass fraction drops below 1 per cent and $M_{\rm CO,20}$ defined as the mass coordinate where the sum of the mass fractions of carbon and oxygen becomes larger than 20 per cent) of the models.

$M_{\rm ini}$	$V_{\rm ini}/V_{\rm crit}$	$M_{\rm fin}$	$M_{\alpha,01}$	$M_{\rm CO,01}$	$M_{\rm CO,20}$
9	0.0	8.80	1.21	1.14	1.15
9	0.4	8.74	1.83	1.31	1.48
12	0.0	11.56	2.98	1.58	1.66
12	0.4	10.36	3.68	2.14	3.06
15	0.0	13.09	4.09	2.24	2.55
15	0.4	10.83	5.22	3.09	4.86
20	0.0	8.45	6.03	3.68	3.96
20	0.4	7.27	7.14	4.66	7.09
25	0.0	8.04	8.04	5.37	6.55
25	0.4	9.08	9.08	6.67	8.95
32	0.0	10.71	10.71	7.77	8.42
32	0.4	9.80	9.80	7.16	9.80
40	0.0	11.33	11.33	8.64	11.33
40	0.4	11.63	11.63	8.97	11.63
60	0.0	10.77	10.77	8.24	10.77
60	0.4	12.87	12.87	9.93	12.87
85	0.0	16.21	16.21	12.91	16.21
85	0.4	16.64	16.64	13.25	16.64
120	0.0	23.40	23.40	19.15	23.40
120	0.4	22.26	22.26	18.05	22.26
150	0.0	30.92	30.92	26.07	30.92
150	0.4	25.79	25.79	21.00	25.79
200	0.0	35.65	35.65	30.02	35.65
200	0.4	34.64	34.64	29.09	34.64
300	0.0	22.23	22.23	18.08	22.23
300	0.4	25.24	25.24	20.62	25.24

using the publicly available Geneva tools.[3] A detailed description of the online tools is presented in Georgy et al. (2014).

3.1 Evolution of surface properties and lifetimes

The evolution of the models in the Hertzsprung–Russell diagram (HRD) is presented in Fig. 1 for the non-rotating (*left*) and rotating (*right*) models. In non-rotating models, the following features can be seen. The MS becomes significantly broader for stars above 30 $M_\odot$ due to the large convective cores and mass-loss during H-burning (see Vink et al. 2010; Castro et al. 2014; Davis et al. 2019; Higgins & Vink 2019; Kaiser et al. 2020; Martinet et al. 2021; Scott et al. 2021, for extended discussions on the MS width for massive stars and CBM). The strong mass-loss in very massive stars (VMS; above 100 $M_\odot$) leads to the tracks converging to the same luminosity range by the end of the MS. The maximum luminosity of RSGs is around $\log_{10}(L/L_\odot) = 5.7$. Stars in the mass range between 25 and 40 $M_\odot$ evolve back to the blue side of the HRD after the RSG phase, while stars below this end their evolution as RSG/AGB/RG. Extended blue loops crossing the Cepheid instability strip occur in models between 5 and 12 $M_\odot$.

Rotation-induced mixing extends the MS lifetime (see Table A1) and luminosity of stars in general. Mixing of helium in the radiative zone above the core can make the MS width narrower (see Martinet et al. 2021), especially for stars with masses above 30 $M_\odot$. The mixing of helium also generally tends to reduce the importance of the H-burning shell and rotating models reach the RSG earlier than non-rotating ones during He-burning (see fig. 3 in Hirschi, Meynet & Maeder 2004). All these effects (coupled with the reduced gravity discussed in the previous section) lead to stronger mass-loss in rotating stars. This shifts the mass ranges mentioned above for non-rotating models to lower initial masses. The maximum luminosity of RSGs is $\log_{10}(L/L_\odot) = 5.5$ with stars around $\log_{10}(L/L_\odot) = 5.6$–5.8 being yellow super/hypergiants (YSG/YHG). Rotating stars from 20 $M_\odot$ upwards evolve back to the blue side of the HRD after the RSG phase. This means that stars with $\log_{10}(L/L_\odot) \sim 5.2$ can occupy the full width of the HRD. This will be further discussed in Section 4. Extended blue loops crossing the Cepheid instability strip occur in rotating models between 7 and 9 $M_\odot$. The colour coding for the nitrogen surface abundance shows that this enrichment occurs already during the MS in rotating models, while it only starts in the cool parts of the HRD for non-rotating stars below 50 $M_\odot$.

Given the strong mass-loss and related angular momentum loss experienced by massive stars at high metallicities, the surface rotation velocity of the models decreases during the MS and the rate of decrease increases with initial mass (see Fig. 2, *left*). Massive stars above 15 $M_\odot$ thus move away from critical rotation (see Fig. 2, *right*). The average surface rotation velocity of massive start on the MS is thus relatively low with $\bar{V}_{\rm MS} \lesssim 200\,{\rm km\,s^{-1}}$ for $M_{\rm ini} \geq 15\,M_\odot$ (and $\bar{V}_{\rm MS} \lesssim 100\,{\rm km\,s^{-1}}$ for $M_{\rm ini} \geq 85\,M_\odot$). In stars below 15 $M_\odot$, internal transport of angular momentum leads models to get slightly closer to critical rotation.

3.2 Evolution of central properties and final total and core masses

Rotation-induced mixing brings additional fuel into convective core and rotating models having generally larger central temperatures and lower central densities, thus behaving in their core like more massive non-rotating stars (see Hirschi et al. 2004). This can be best seen in Fig. 3 by comparing the tracks of the 12 $M_\odot$ models in the partially degenerate section of the central temperature versus central density diagram. The convergence of the evolution tracks observed in the HRD for VMS is also observed in this diagram (for the same reason: strong mass-loss).

The final total mass along with core masses of the models are listed in Table 2 and plotted in Fig. 4. The strong mass-loss experienced by high-metallicity stars leads to final total masses being much lower than initial masses for both non-rotating and rotating stars. The maximum final mass in the entire grid is 36 $M_\odot$ for the 200 $M_\odot$ non-rotating model. The maximum final total mass for rotating models is very similar (35 $M_\odot$ for the rotating 200 $M_\odot$ model). It is interesting to note that further increasing the initial mass of the model does not lead to an increase in the final mass (the 300 $M_\odot$ models have final masses smaller than 26 $M_\odot$). This is due to the strong luminosity dependence of mass-loss rates. While there are still uncertainties related to mass-loss (especially in the cool part of the HRD), it is very unlikely that stars would be able to retain more than 40 $M_\odot$ at supersolar metallicity and this would also represent an upper limit for black hole masses coming from single stars at this metallicity.[4]

Related to this, the models do not predict any pair-instability supernova at supersolar metallicity.

[3] https://obswww.unige.ch/Recherche/evoldb/index/

[4] Much larger BH masses are predicted at lower metallicities (see e.g. Umeda et al. 2020; Farrell et al. 2021; Vink et al. 2021).

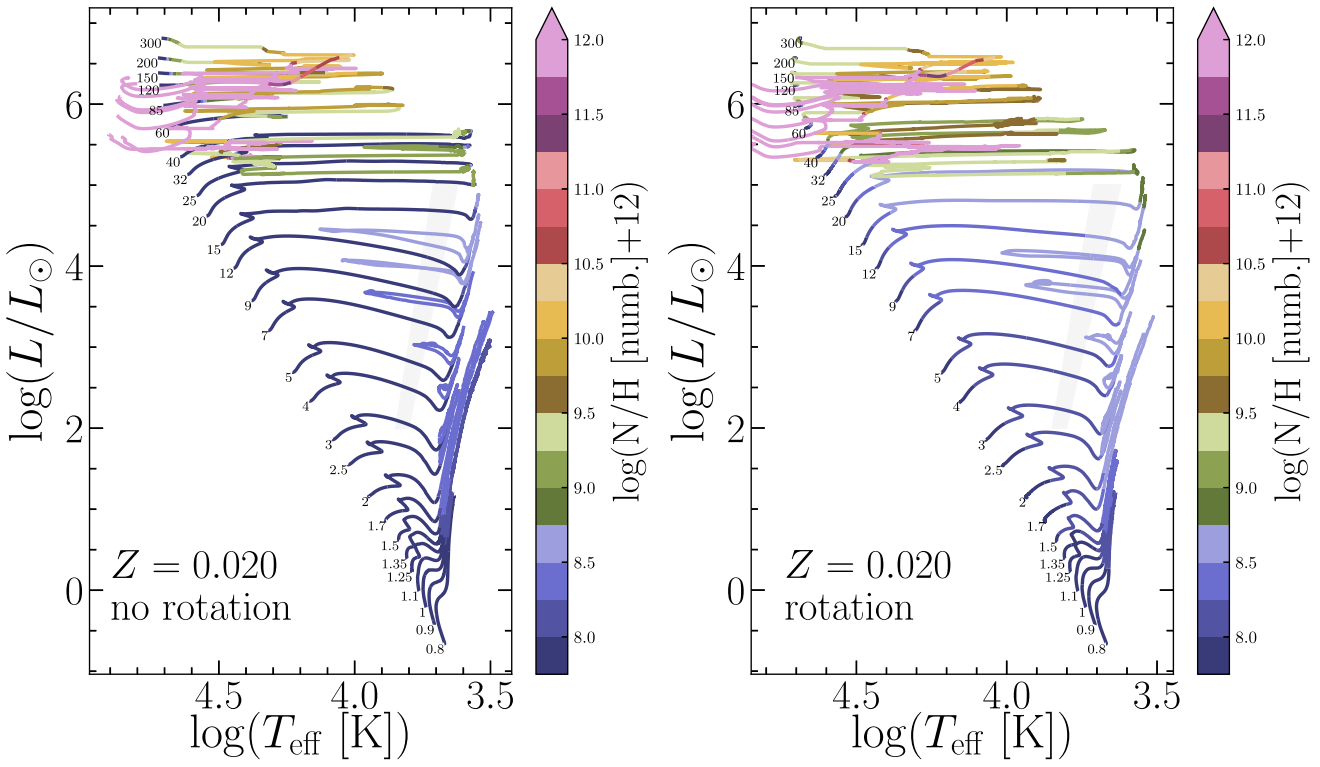

Figure 1. HR diagram for the non-rotating (*left*) and rotating (*right*) models at $Z = 0.020$. Colour coded is the surface nitrogen abundance in $\log(N/H) + 12$. Note that the effective temperature used throughout the paper is the temperature at the surface of the star. The corrected temperature for thick winds is available in the electronic tables (see link at the end of the paper).

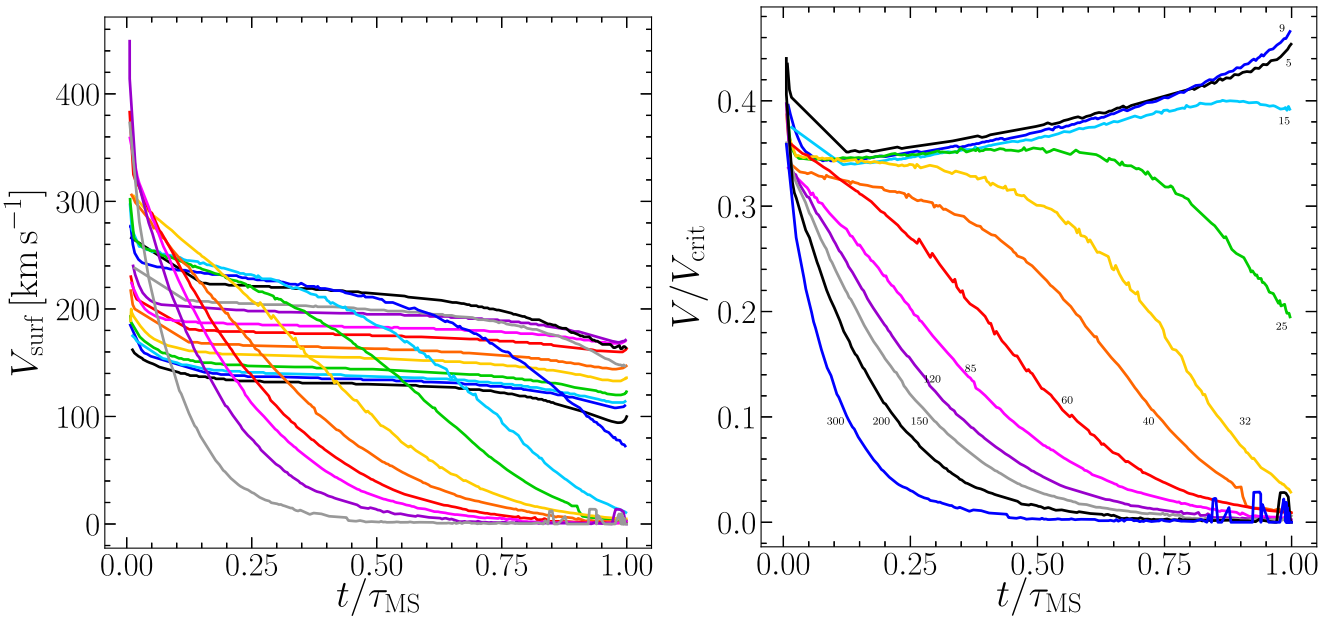

Figure 2. Velocity evolution of the rotating models at $Z = 0.020$ as a function of the MS lifetime. *Left:* surface velocity. Stars from 1.7 (lowest track at $t/\tau_{MS} = 0$) to 300 $M_\odot$. *Right:* ratio V/V_{crit} of selected massive star models.

Comparing the total and helium core (M_α) masses, one can see that mass-loss is strong enough in stars above 20 $M_\odot$ for rotating stars (25 $M_\odot$ for non-rotating stars) to remove the entire hydrogen-rich envelope. Our models thus predict SNII below 20 $M_\odot$ for rotating stars (25 $M_\odot$ for non-rotating stars) and SNIb above that. We provide two values for the carbon-oxygen core masses. $M_{CO,01}$ is defined as the mass coordinate where the helium mass fraction drops below 1 per cent. It roughly corresponds to the maximum mass reached by

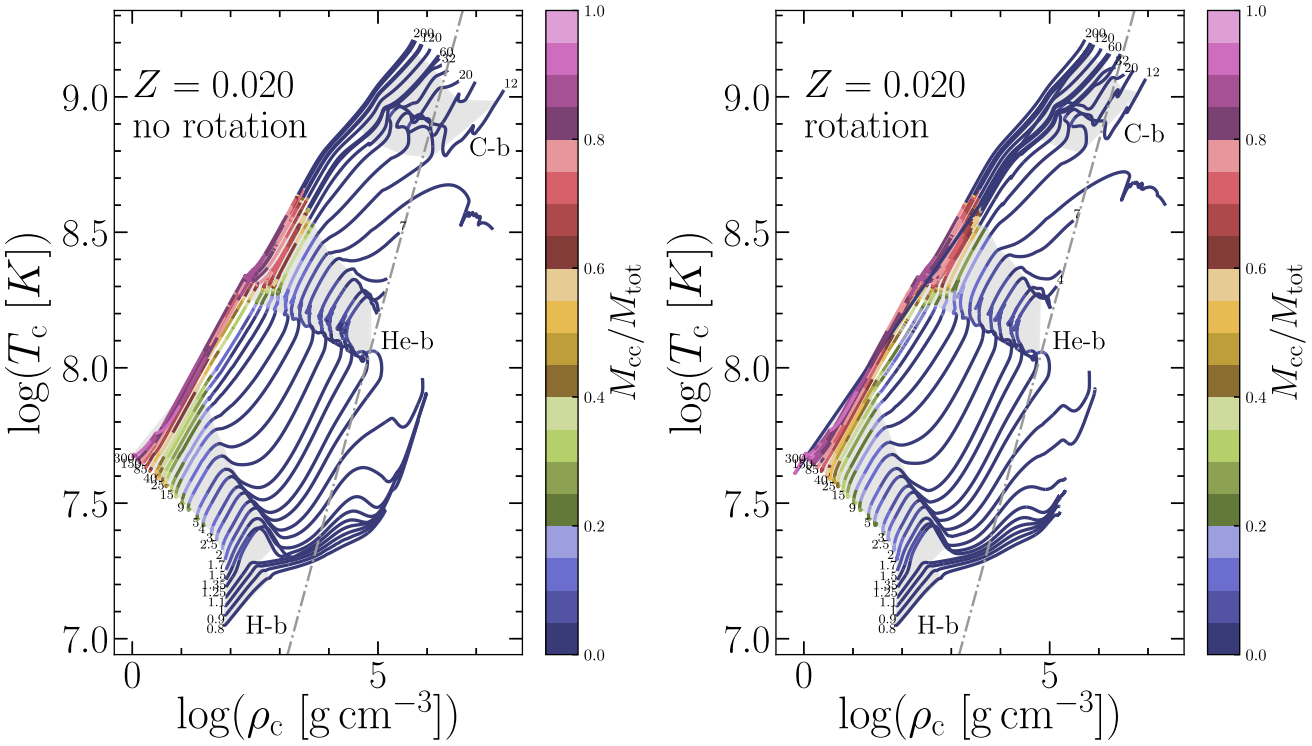

Figure 3. Central temperature (T_c) versus central density (ρ_c) diagram for the non-rotating (*left*) and rotating (*right*) models at $Z = 0.020$. Colour coded is the fractional mass (M_{cc}/M_{tot}) of the convective core. The dot–dashed line indicates the transition from non-degenerate to partially degenerate conditions.

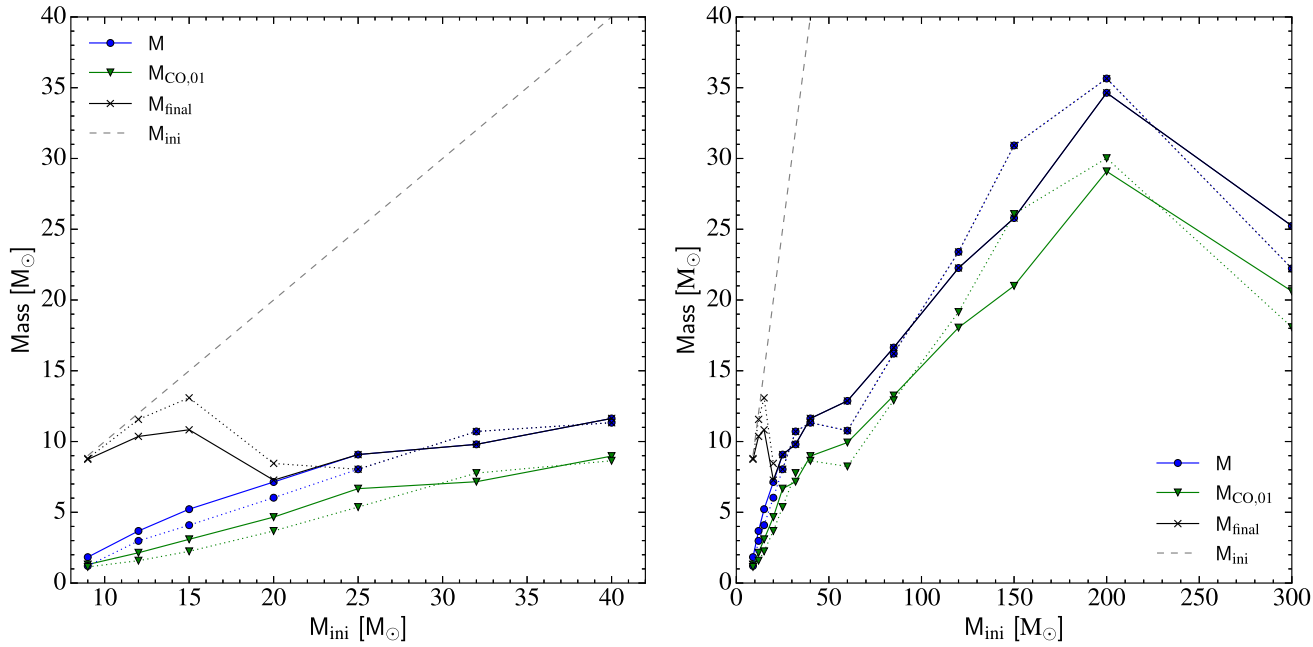

Figure 4. Helium-core ($M_{\alpha,01}$ defined as the mass coordinate where the hydrogen mass fraction drops below 1 per cent) and carbon-oxygen core masses ($M_{CO,01}$ defined as the mass coordinate where the helium mass fraction drops below 1 per cent and $M_{CO,20}$ defined as the mass coordinate where the sum of the mass fractions of carbon and oxygen becomes larger than 20 per cent) of the models. Straight line is for rotating model and dotted line is for non-rotating model. *Left*: zoom in on the mass range from 9 to 40 $M_\odot$. *Right*: the full mass range from 9 to 300 $M_\odot$.

the convective core during core helium burning. It is also the location of a steep density gradient at the edge of that core. This gradient will help the SN shock-wave to eject material above that point and it is thus our recommended value for the CO core mass of our models. There are different ways of determining core masses from stellar models (see e.g. Hirschi et al. 2004). We thus also provide another measure of the CO-core mass, $M_{CO,20}$, defined as the first mass coordinate moving from the surface to the centre where the sum of the mass

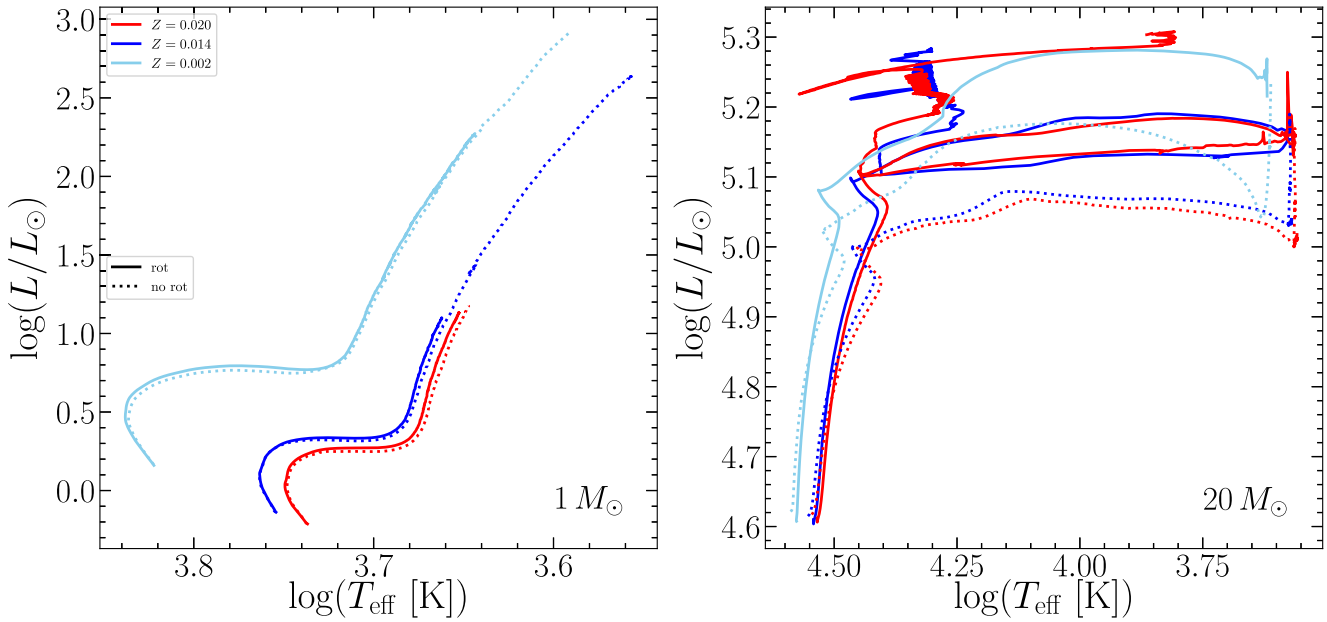

Figure 5. HR diagrams for 1 (*left*), and 20 $M_\odot$ (*right*) models with and without rotation, at $Z = 0.020$ (red), $Z = 0.014$ (dark blue; Ekström et al. 2012), and $Z = 0.002$ (sky blue; Georgy et al. 2013).

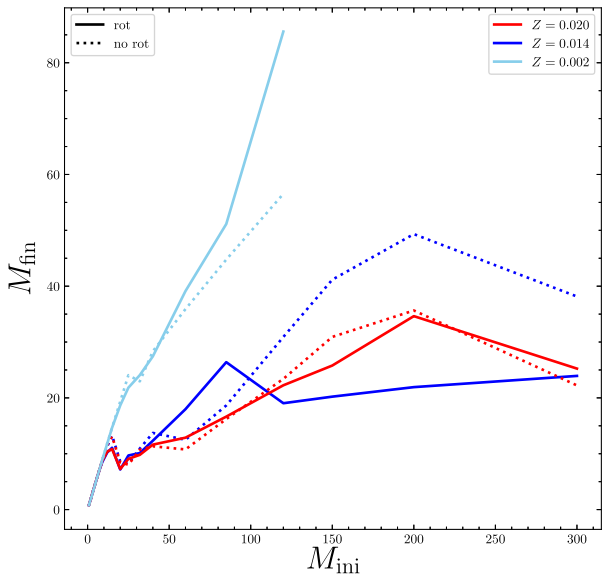

Figure 6. Final mass as a function of initial mass for models with and without rotation at $Z = 0.020$ (red), $Z = 0.014$ (dark blue; Ekström et al. 2012; Yusof et al. 2013, for $M_{\rm ini} > 120$ $M_\odot$), and $Z = 0.002$ (sky blue; Georgy et al. 2013).

fractions of carbon and oxygen becomes larger than 20 per cent. In hydrogen-rich models, this definition falls in between M_α and $M_{\rm CO,01}$. For H-free models, $M_{\rm CO,20}$ usually includes the helium burning shell layer, which is composed of helium, carbon, and oxygen in various ratios and is thus equal to M_α. One could wrongly conclude that there is no helium left in these models. This discussion also demonstrates that it is important to use a comparable definition to compare different grids of models. Comparing M_α and $M_{\rm CO,01}$, we see that the models all retain several solar masses of helium-rich material (the helium surface abundance is given in Table A1). It is still debated (see e.g. Dessart et al. 2020, and references therein) whether some (and how much) helium can be hidden in SNIc. If helium cannot be hidden, then our models would not predict any SNIc at supersolar metallicity, only SNII up to about 20 $M_\odot$ for rotating stars (25 $M_\odot$ for non-rotating stars) and SNIb above that (using the mass-loss prescriptions described in Section 2).

3.3 Comparison to Geneva grids at other metallicities

Given the modest difference in metallicity between the supersolar and solar metallicity models (43 per cent), it is expected that the models at both metallicities have a qualitatively similar evolution, which is indeed the case when comparing most properties of the grids of models. As discussed in Section 1, it is nevertheless very useful to have a grid of models tailored to the metallicity of the Galactic Centre to first confirm expectations and second avoid the reliance on extrapolation of model properties to a different metallicity. We expect the effects of metallicity in supersolar metallicity models to be in the opposite direction to the effects in low-metallicity models. This is confirmed for the evolutionary tracks in the HRD as can be seen for the 1 and 20 $M_\odot$ models in Fig. 5 presenting non-rotating and rotating models at $Z = 0.020$, 0.014, and 0.002. The figure shows that the higher the metallicity, the cooler and slightly less luminous the tracks on the MS (explained mainly by the higher opacity at higher metallicity). This leads to slightly longer MS lifetimes (by 20 per cent or less) for supersolar models compared to solar metallicity models.

Mass-loss is one of the properties of stellar models most affected by metallicity. While the dependence of mass-loss on metallicity varies according to the location of the star in the HRD (see Section 2 for details), the general trend is that mass-loss is higher at higher metallicity, which leads to lower final masses. The final masses of the $Z = 0.020$ models are compared to models at $Z = 0.014$ and 0.002 in Fig. 6. While supersolar metallicity models lose much more mass than low-Z models, final masses are similar to solar metallicity models up to 30 $M_\odot$. This can be explained by several factors: first the proximity in metallicity between the two grids, second the

fact that the models do not include a metallicity dependence for $\log_{10}(T_{\rm eff}/K) < 3.7$, and third the dependence of mass-loss rates on luminosity. The second factor plays an important role for stars in the 15 to 30 $M_\odot$ range since stars in this range lose most mass as very cool RSGs. The third factor plays a dominant role for VMS as discussed above. Indeed, VMS are so luminous that they lose a lot of mass. This reduces the luminosity of the star, which in turn reduces its mass-loss. The maximum final mass of the supersolar models around 35 $M_\odot$ is lower than the maximum mass of 49.3 $M_\odot$ (for the 200 $M_\odot$ from Yusof et al. 2013) retained by non-rotating solar metallicity models while it is higher than the maximum mass reached by rotating solar metallicity models of 26.4 $M_\odot$ (for the 85 $M_\odot$ model from Ekström et al. 2012). The maximum mass retained depends both on the evolutionary path taken by the VMS models (non-rotating models reach cooler temperatures than rotating ones) and the mass-loss experienced during the various phases. An important finding from our models is that starting from an even higher initial mass would not allow high-metallicity stars to produce more massive black holes (no black hole masses predicted above 50 $M_\odot$ for solar or higher metallicities). This confirms that at high metallicity mass-loss is the major process determining the maximum mass of black holes from single stars. The models would thus not predict pair-instability SNe at solar or supersolar metallicities. As can be seen from the $Z = 0.002$ models, this is not the case at sub-solar metallicities (see also Eggenberger et al. 2021; Higgins et al. 2021, and references therein).

4 COMPARISON TO OBSERVATIONS

As discussed in Section 1, there are several massive young clusters in the inner Galactic disc. The best-studied massive young star cluster in the inner Galactic disc is Wd1, at a distance of ∼4 kpc (Beasor et al. 2021), while there are also several older massive clusters at the end of the Galactic Bar which are rich in red supergiants (Davies et al. 2009). Wd1 (Westerlund 1961) is perhaps the richest young star cluster within the disc of the Milky Way. Clark et al. (2005) first highlighted its exceptional population of both hot and cool evolved massive stars, arising from its high cluster mass, $\sim 10^5$ $M_\odot$. The simultaneous presence of WR stars (WN and WC) and cool supergiants led to a preferred age of ∼4–5 Myr (Crowther et al. 2006) based on predictions from single star evolutionary models, although Beasor et al. (2021) have recently reassessed the age of Wd1 on the basis of its cool supergiant population and argue for an older age of ∼10 Myr. Unfortunately, the metallicity of Wd1 is not known, since gas associated with the formation of the cluster has been dispersed. This prevents standard nebular diagnostics, and the usual present-day stellar diagnostics (iron lines in blue spectra of B-type stars) are inaccessible owing to high foreground extinction ($A_V \sim 13$ mag; Clark et al. 2005).

Within the Galactic Centre (Gravity Collaboration 2019), there are several young high mass ($\geq 10^4$ $M_\odot$) clusters including the Arches, Quintuplet, and Galactic Centre clusters, plus a rich massive star population within the Central Molecular Zone (Clark et al. 2021).

The Arches cluster is the youngest, densest star cluster in the vicinity of the Galactic Centre. It was discovered independently by Nagata et al. (1995) and Cotera et al. (1996). It hosts a rich population of O stars and hydrogen rich WN stars (Martins et al. 2008; Clark et al. 2019), such that its age is 2–3 Myr. The Quintuplet cluster is somewhat older than the Arches since it hosts late O supergiants, WC and WN-type WR stars plus Luminous Blue Variables, with an age of 3–5 Myr from comparison with single star models (Liermann et al. 2009; Clark et al. 2018b). Standard nebular and stellar abundance diagnostics are also challenging for massive stars in the Galactic Centre due to extreme visual extinction, although Cunha et al. (2007) have analysed intermediate to high mass cool supergiants in the central cluster and Quintuplet to reveal iron abundances 0.10 to 0.15 dex higher than the solar value, with [O/Fe]∼ 0.2 dex. Najarro et al. (2009, 2014) have obtained similar results for selected early-type stars in the Quintuplet cluster.

We will mainly compare our supersolar metallicity models to the massive stars observed in Wd1 since it is the best-studied young metal-rich cluster. We will also briefly compare our models to observed stars in the Arches and Quintuplet clusters.

In order to estimate the ages of these clusters, we compare the isochrones of our supersolar models to the observed massive star populations in Fig. 7. Starting with the Arches and Quintuplets clusters, we see that luminous stars in these clusters (Martins et al. 2008; Liermann et al. 2010) fall between the isochrones with $\log_{10}(\text{age/yr}) = 6.3$ and 6.5. These values match previous age estimates for the Arches cluster (2–3 Myr; Martins et al. 2008; Clark et al. 2018a) and are close to prior age estimates for the Quintuplet cluster (3–5 Myr; Liermann, Hamann & Oskinova 2012; Clark et al. 2018b). Comparing the observations to the evolutionary tracks of our models (not shown here), late WN stars in the Quintuplet cluster have initial masses above 80 $M_\odot$, although neither O stars nor (dusty) WC stars have been subject to quantitative investigation to date, hindering a more refined age determination. For the Arches cluster (and indirectly other Galactic Centre clusters), Clark et al. (2018a) have emphasized the sensitivity of stellar luminosities to the adopted extinction law. The discovery of a very high mass binary system (F2) in the Arches cluster (Lohr et al. 2018) favours its youth with respect to alternative interpretations involving the most massive stars being the products of binary evolution (Schneider et al. 2014). More detailed studies would be needed to provide precise information on these clusters, consequently we will focus on Wd1 for the rest of the comparisons.

Extensive spectroscopic studies of the massive star population in Wd1 have been undertaken since this cluster first came to prominence (Clark et al. 2005), although in common with the Galactic Centre clusters, quantitative spectroscopic results have not been undertaken for OB stars in Wd1. The simultaneous presence of WR stars and cool supergiants led Clark et al. (2005) to conclude that its age was 3.5–5 Myr. Crowther et al. (2006) provided estimates of the physical properties of WR stars in Wd1, from which a cluster age of ∼5 Myr was favoured from comparison with predictions from single stars. Rosslowe (2016) undertook a more detailed analysis of the WR population of Wd1, taking into account contributions from binary companions and hot dust emission. Negueruela, Clark & Ritchie (2010) favoured $\log_{10}(\text{age/yr}) = 6.7$ to 6.8 from a comparison between its rich OB supergiant population and previous generations of Geneva single star models, with its youth reinforced from the detection of high mass eclipsing binaries (Ritchie et al. 2010). In contrast, Beasor et al. (2021) have reassessed the luminosities of cool supergiants in Wd1 incorporating mid-IR photometry to infer a substantially older age of ∼10 Myr.

From the comparison between the physical properties of WR stars and cool supergiants in Wd1 to new isochrones in Fig. 7, we see that non-rotating models at $\log_{10}(\text{age/yr})$ around 6.7 reach the position of the WR stars, although the luminosity of the models is slightly too high. Non-rotating models at $\log_{10}(\text{age/yr})$ around 6.9 overlap with the position of the red and yellow supergiants (RSG and YSG) from Beasor et al. (2021). Rotating models on the other end, reach the position of the WR stars at $\log_{10}(\text{age/yr})$ around 6.8–6.9 while they cover the region occupied by the RSGs and YSGs for $\log_{10}(\text{age/yr})$ around 7.0.

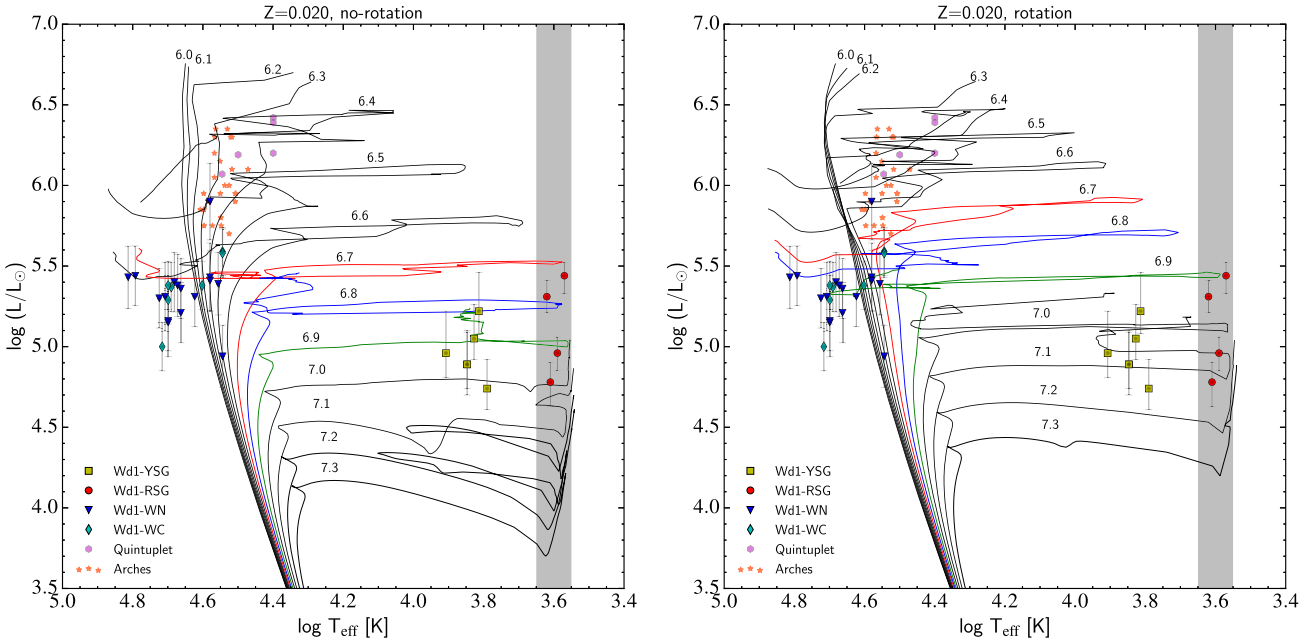

Figure 7. HR diagram comparing cool supergiants in Wd1 (red circles for RSG, yellow squares for YSG; Beasor et al. 2021) and hot, luminous stars in the Wd 1 (blue inverted triangles for WN stars, cyan diamonds for WC stars; Rosslowe 2016), Arches (orange stars; Martins et al. 2008) and Quintuplet (pink hexagons; Liermann et al. 2010) clusters to the supersolar metallicity isochrones for non-rotating (*left*) and rotating (*right*) models. The number along or at the end of the isochrones corresponds to the $\log_{10}$ of the age of the isochrone. Isochrones with $\log_{10}$(age/yr) = 6.7, 6.8, and 6.9 are coloured in red, blue, and green, respectively, to facilitate the comparisons. The grey shaded area indicates the temperature range for the observed RSG stars.

To find out the initial masses of the models reaching the observed position of Wd1 stars, we compare observations to evolutionary tracks of our supersolar models between 15 and 60 $M_\odot$ in Fig. 8. We see that non-rotating models with $M_{\rm ini}$ above 25 $M_\odot$ reach the position of the WR stars in Wd1 (though again the luminosity of the models is slightly higher than that of the observed WR stars), while non-rotating models with $M_{\rm ini}$ between 15 and 32 $M_\odot$ overlap with the position of the red and yellow supergiants (RSG and YSG). Rotating models with $M_{\rm ini}$ above 20 $M_\odot$ reach the position of the WR stars in Wd1 while they cover the region occupied by the RSGs and YSGs for $M_{\rm ini}$ between 15 and 25 $M_\odot$.

As already discussed in Section 3, the mass range of these models corresponds to the transition between stars ending as RSGs (and SNII) and those ending as WRs (SNIb/c). In both the models and Wd1 stars, this transition occurs for $\log_{10}(L/L_\odot)$ = 5–5.5 (possibly at a slightly lower luminosity in Wd1 stars compared to the models).

To take the comparison one step further, we used the SYCLIST tool (see Georgy et al. 2014, for details) to generate synthetic clusters out of the supersolar models. The estimated total stellar mass of Wd1 is $\sim 10^5$ $M_\odot$. Using a Salpeter IMF with the lower and upper mass bounds from the grids (0.8 and 300 $M_\odot$, respectively) yields an average mass of $\sim$ 2.6 $M_\odot$. We thus generated clusters initially containing 40 000 stars in total. To take into account the age estimates ranging from about 5 to 10 Myr from the above comparison to isochrones (as well as age determinations from the literature; Clark et al. 2005; Crowther et al. 2006; Beasor et al. 2021) and the possibility of a cluster formation event lasting a few million years, we computed four clusters with $\log_{10}$(age/yr) = 6.7, 6.8, 6.9, 7.0, each with 10 000 initial stars. We construct such clusters for both the non-rotating (Fig. 9) and the rotating (Fig. 10) models. Note that while there are initially 40 000 stars in the clusters, the most massive stars will have died by the age at which we compute the clusters. Thus, the total mass of the synthetic clusters is slightly below 10^5 $M_\odot$. We also make a more realistic cluster with mixed rotation, initially containing 7000 × 4 non-rotating and 3000 × 4 rotating stars (Fig. 11). For this 'mixed rotation' cluster we add Gaussian noise on L and $T_{\rm eff}$ to simulate observed stars (σ_L = 0.2 dex, $\sigma_{T_{\rm eff}}$ = 0.05 dex).

Fig. 9 shows that the non-rotating clusters are able to broadly reproduce the observed RSGs and YSGs in Wd1. However, they produce too few WR stars and those produced possess $T_{\rm eff}$ and $\log_{10}(L/L_\odot)$ about 0.3 dex too high compared to observations (most visible in the *left-hand* panels). On the other hand, the rotating clusters (Fig. 10) yield a better agreement with the observed WR population. This is explained by the rotating 20–25 $M_\odot$ models becoming WR stars with $\log_{10}(L/L_\odot)$ ∼5.2 [especially around $\log_{10}$(age/yr) = 6.9]. Rotating models predict fewer RSG/YSG than non-rotating models and the predicted 'YSG' have higher effective temperatures than typical YSGs (note, however, that the effective temperature of the YSG/RSGs in Wd1 is not very precise so one cannot draw firm conclusions on this point). Finally, the cluster with mixed rotation (right-hand panel of Fig. 11) is able to qualitatively reproduce the existence of various evolved sub-types at the observed luminosities.

The comparison is not perfect, however, especially when considering the relative number of stars in the various sub-types. Indeed, the synthetic cluster contains more RSG and YSG and less WR stars than what is observed. A perfect match was not expected for several reasons. First, the parameters chosen for the synthetic clusters are based on estimates for the total cluster mass, the SFR and the distribution of initial stellar rotation and these are uncertain. For example, the cluster formation history of Westerlund-1 is probably not as simple as four independent and identical star formation episodes. If, for instance, its SFR increased over time, we should expect to see relatively more WR stars and fewer RSG and YSG

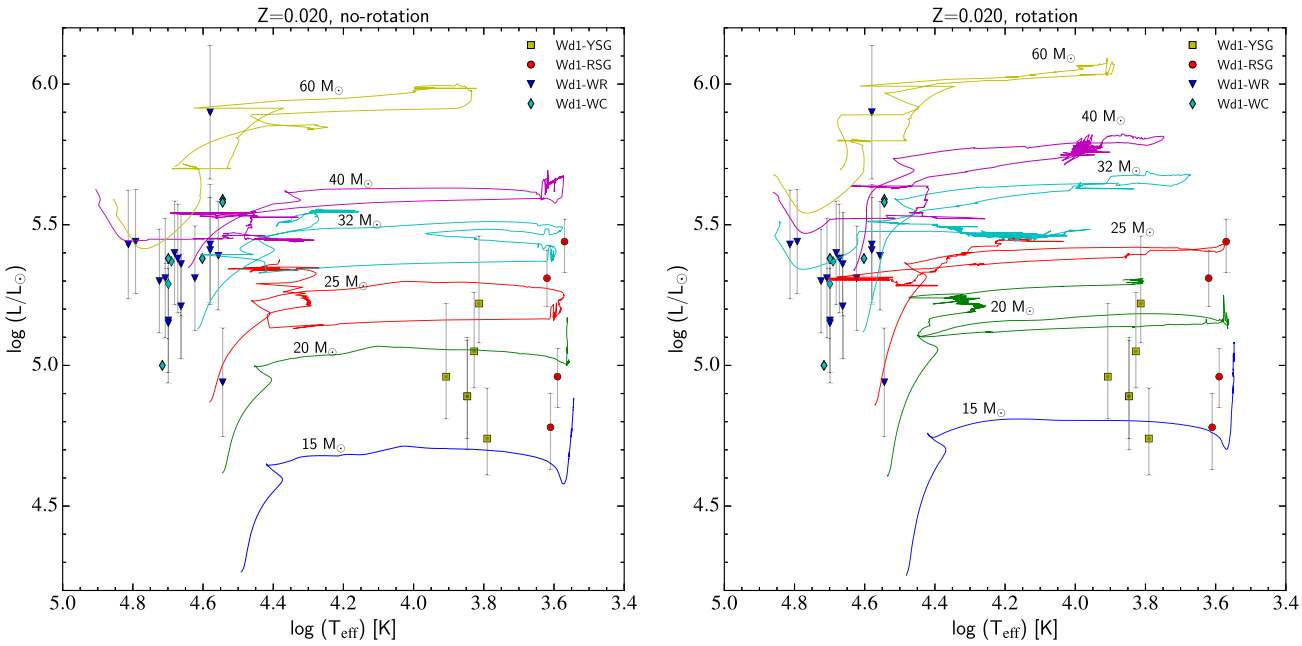

Figure 8. Comparison in the HRD of the evolutionary tracks of the 15 to 60 $M_\odot$, non-rotating (*left*) and rotating models (*right*) to the Wd1 data (same Wd1 data as in Fig. 7).

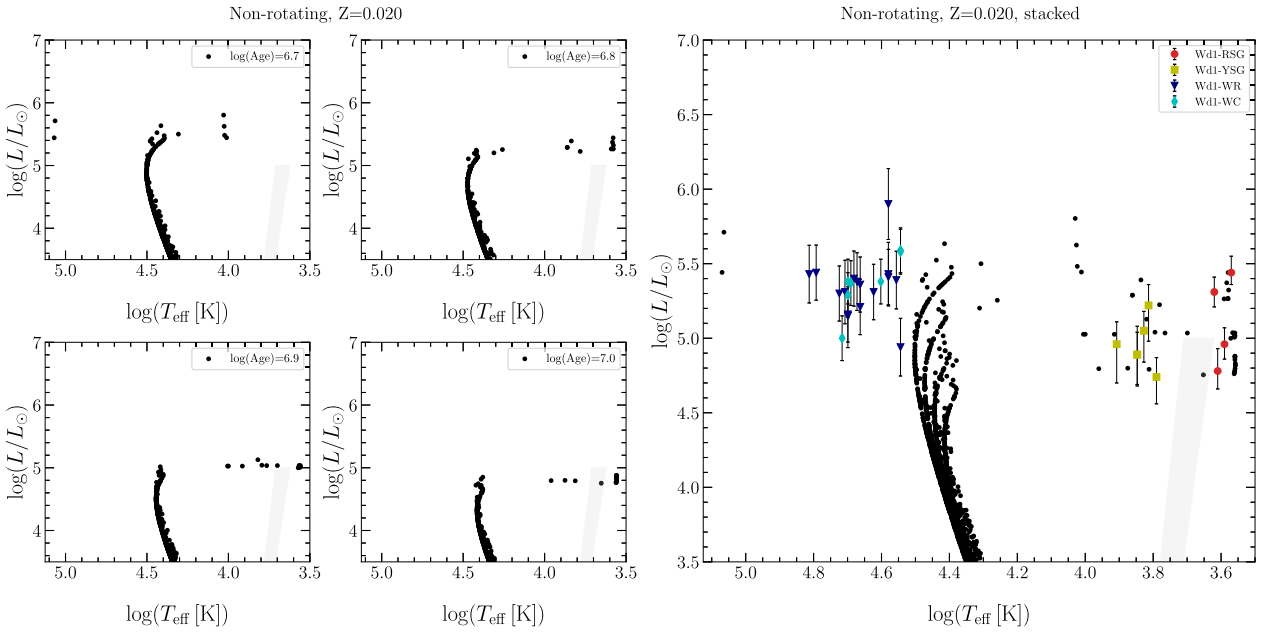

Figure 9. HRD of synthetic clusters with log10(age/yr)= 6.7, 6.8, 6.9, 7.0, at Z=0.020, each with 10,000 initial stars, without rotation. *Left:* Individual 10,000-star clusters considering instantaneous star formation. *Right:* Cluster of 40,000 initial stars combining (stacking) the stars from the four 10,000-star individual clusters on the left, corresponding to a star formation episode lasting 5 Myr.

stars compared to our constant SFR cluster. Secondly, the grid of models only includes single stars so we would expect binary interactions to contribute to the WR stars. This being said, Beasor et al. (2021) are unable to fit their observations with a single-aged BPASS model (Stanway & Eldridge 2018). Thirdly, another uncertainty concerns mass-loss. In particular, mass-loss prescriptions on the cool side of the HRD are all empirical (see Section 2 for details). Beasor et al. (2021) compare their observations to the MIST isochrones of Choi et al. (2016). The MIST and Geneva isochrones are very different above $\log_{10}(L/L_\odot) \gtrsim 5$. The MIST isochrones never reach effective temperatures above $\log_{10}(T_{\rm eff}) > 4.2$ for $\log_{10}(L/L_\odot) < 6.0$ (or ages larger than 4.5 Myr), whereas our isochrones cross back the MS at $\log_{10}(L/L_\odot) \sim 5.5$ (or below), for our non-rotating models. Evolutionary tracks of MIST models

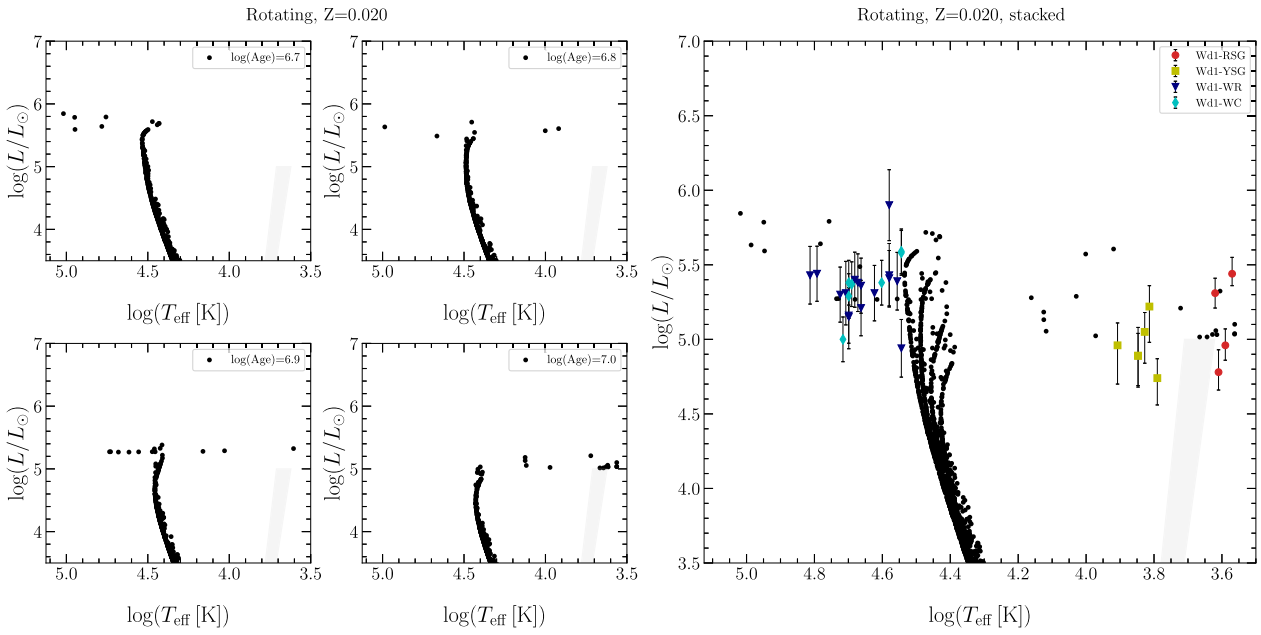

Figure 10. Same as Fig. 9 but for rotating models.

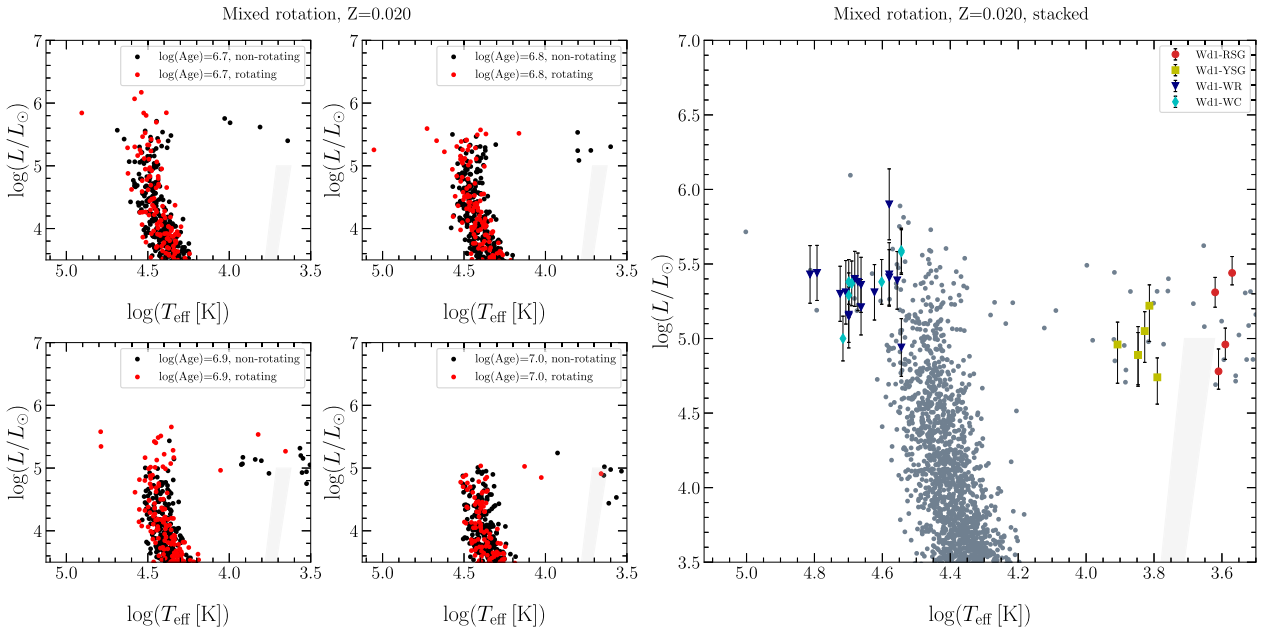

Figure 11. HRD of synthetic clusters of log (age/yr) 6.7, 6.8, 6.9, 7.0, at Z = 0.020, each containing 10 000 initial stars with mixed rotation: 7000 without rotation (black dots) and 3000 with rotation (red dots). We added Gaussian noise on L and $T_{\rm eff}$ to simulate observed stars ($\sigma_L = 0.2$ dex,$\sigma_{\rm Teff} = 0.05$ dex). *Left:* Individual 10 000-star clusters considering instantaneous (or very brief) star formation. *Right:* Cluster of 40 000 initial stars combining the stars from the four 10 000-star individual clusters on the left, corresponding to a star formation episode lasting 5 Myr.

for the 15–60 $M_\odot$ rotating models at [Fe/H]+0.25 ($Z = 0.0254$) are shown in Fig. 12. These show that these MIST supersolar metallicity models up to 40 $M_\odot$ never leave the RSG phase (even considering rotation) so retain at least part of their H-rich envelope. The MIST stellar models have various ingredients that are different from the Geneva models used here (e.g. different implementation of rotation-induced mixing) so it is not straightforward to extract the impact of the mass-loss uncertainties. This being said, the difference between MIST and GENEVA models in the 20–40 $M_\odot$ mass range is most likely dominated by differences in mass-loss in the RSG phase. The comparison to Wd1 provides support for significant mass-loss in the RSG phase for this mass range, thus probably for an enhanced mass-loss rate when the sub-surface or surface layers approach the Eddington limit, which is implemented in our models (see Section 2 for details). Generally, this confirms the importance of mass-loss and of the related uncertainties for evolution of massive stars. Taking

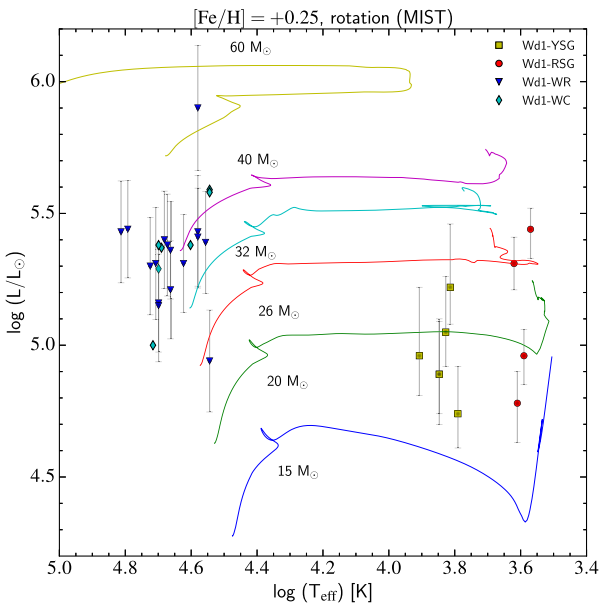

Figure 12. Comparison in the HRD of MIST evolutionary tracks for the $15-60 M_{\odot}$ rotating models at [Fe/H]+0.25 ($Z = 0.0254$) to the Wd1 data (same Wd1 data as in Fig. 7).

all these factors into considerations, the present grid of single star models (with its physical ingredients described in Section 2) is able to reproduce the Wd1 evolved populations rather well, at least qualitatively.

5 CONCLUSIONS

In this paper, we present a grid of stellar models at supersolar metallicity ($Z = 0.020$) covering a wide range of initial masses from 0.8 to 300 $M_{\odot}$. This grid extends the previous grids of Geneva models at solar and sub-solar metallicities (Ekström et al. 2012; Georgy et al. 2013; Groh et al. 2019; Eggenberger et al. 2021; Murphy et al. 2021) and thus uses the same physical ingredients and metallicity dependences. A metallicity of $Z = 0.020$ was chosen to match that of the inner Galactic disc. After presenting the models, we compare them to Geneva grids at other metallicities and several massive young stellar clusters near the Galactic centre, Wd1, in particular.

A modest increase of 43 per cent (= 0.02/0.014) in metallicity compared to solar models means that the models evolve similarly to solar models but with slightly larger mass-loss rates. Mass-loss limits the final total mass of the supersolar models to 35 $M_{\odot}$, even for stars with initial masses much larger than 100 $M_{\odot}$. Thus, the models would predict neither pair-instability supernovae nor BHs above 35 $M_{\odot}$ at supersolar metallicity. Furthermore, mass-loss is strong enough in stars above 20 $M_{\odot}$ for rotating stars (25 $M_{\odot}$ for non-rotating stars) to remove the entire hydrogen-rich envelope. Our models thus predict SNII below 20 $M_{\odot}$ for rotating stars (25 $M_{\odot}$ for non-rotating stars) and SNIb (possibly SNIc) above that.

We computed both isochrones and synthetic clusters to compare our supersolar models to the Wd1 massive young cluster. A synthetic cluster combining rotating and non-rotating models with an age spread between $\log(\text{age/yr}) = 6.7$ and 7.0 is able to reproduce qualitatively the observed populations of WR, YSG, and RSG stars in Wd1. In particular, the models are able to reproduce the simultaneous presence of WR, YSG, and RSG stars at $\log_{10}(L/L_{\odot})$ 5–5.5. The quantitative agreement is not perfect though and we discuss the likely causes: synthetic cluster parameters, binary interactions and mass-loss and the related uncertainties. In particular, mass-loss in the cool part of the HRD plays a key role (as demonstrated by the different predictions between this study and Choi et al. 2016). Furthermore, larger CBM supported by various studies (see e.g. Scott et al. 2021, and references therein) would likely lower the minimum initial mass of a single star to produce a WR star.

ACKNOWLEDGEMENTS

NY and HAK acknowledge the Fundamental Research Grant Scheme grant number FP042-2018A and FP045-2021 under Ministry of Higher Education, Malaysia. HAK would like to thank Astrophysics Group, Keele University for hosting his sabbatical where part of this work has been done. RH acknowledges support from the World Premier International Research Centre Initiative (WPI Initiative, MEXT, Japan), STFC UK, the European Union's Horizon 2020 research and innovation programme under grant agreement No. 101008324 (ChETEC-INFRA) and the IReNA AccelNet Network of Networks, supported by the National Science Foundation under Grant No. OISE-1927130. This article is based upon work from the ChETEC COST Action (CA16117), supported by COST (European Cooperation in Science and Technology). PE, SE, CG, YS, and GM have received funding from the European Research Council (ERC) under the European Union's Horizon 2020 research and innovation programme (grant agreement No. 833925, project STAREX). JHG, EF, and LM wish to acknowledge the Irish Research Council for funding this research.

DATA AVAILABILITY

An interactive tool to access the models can be found at this address: https://www.unige.ch/sciences/astro/evolution/en/database/. Additional data requests can be made to the corresponding author.

REFERENCES

Asplund M., 2005, ARA&A, 43, 481
Asplund M., Grevesse N., Sauval A. J., 2005, in Barnes Thomas G. I., Bash F. N., eds, ASP Conf. Ser. Vol. 336, Cosmic Abundances as Records of Stellar Evolution and Nucleosynthesis. Astron. Soc. Pac., San Francisco, p. 25
Asplund M., Grevesse N., Sauval A. J., Scott P., 2009, ARA&A, 47, 481
Asplund M., Amarsi A. M., Grevesse N., 2021, A&A, 653, A141
Balser D. S., Rood R. T., Bania T. M., Anderson L. D., 2011, ApJ, 738, 27
Beasor E. R., Davies B., Smith N., Gehrz R. D., Figer D. F., 2021, ApJ, 912, 16
Bresolin F., Schaerer D., González Delgado R. M., Stasińska G., 2005, A&A, 441, 981
Bresolin F., Kudritzki R.-P., Urbaneja M. A., Gieren W., Ho I. T., Pietrzyński G., 2016, ApJ, 830, 64
Bressan A., Marigo P., Girardi L., Salasnich B., Dal Cero C., Rubele S., Nanni A., 2012, MNRAS, 427, 127
Brott I. et al., 2011, A&A, 530, A115
Caffau E., Ludwig H.-G., Steffen M., Freytag B., Bonifacio P., 2011, Sol. Phys., 268, 255
Castro N., Fossati L., Langer N., Simón-Díaz S., Schneider F. R. N., Izzard R. G., 2014, A&A, 570, L13
Chen Y., Bressan A., Girardi L., Marigo P., Kong X., Lanza A., 2015, MNRAS, 452, 1068
Choi J., Dotter A., Conroy C., Cantiello M., Paxton B., Johnson B. D., 2016, ApJ, 823, 102

Clark J., Negueruela I., Crowther P., Goodwin S., 2005, A&A, 434, 949
Clark J. S., Lohr M. E., Najarro F., Dong H., Martins F., 2018a, A&A, 617, A65
Clark J. S., Lohr M. E., Patrick L. R., Najarro F., Dong H., Figer D. F., 2018b, A&A, 618, A2
Clark J. S., Lohr M. E., Patrick L. R., Najarro F., 2019, A&A, 623, A84
Clark J. S., Patrick L. R., Najarro F., Evans C. J., Lohr M., 2021, A&A, 649, A43
Cotera A. S., Erickson E. F., Colgan S. W. J., Simpson J. P., Allen D. A., Burton M. G., 1996, ApJ, 461, 750
Crowther P. A., 2000, A&A, 356, 191
Crowther P. A., Hadfield L., Clark J., Negueruela I., Vacca W., 2006, MNRAS, 372, 1407
Cunha K., Hubeny I., Lanz T., 2006, ApJ, 647, L143
Cunha K., Sellgren K., Smith V. V., Ramirez S. V., Blum R. D., Terndrup D. M., 2007, ApJ, 669, 1011
Davies B., Origlia L., Kudritzki R.-P., Figer D. F., Rich R. M., Najarro F., Negueruela I., Clark J. S., 2009, ApJ, 696, 2014
Davis A., Jones S., Herwig F., 2019, MNRAS, 484, 3921
de Jager C., Nieuwenhuijzen H., van der Hucht K. A., 1988, A&AS, 72, 259
Dessart L., Yoon S.-C., Aguilera-Dena D. R., Langer N., 2020, A&A, 642, A106
Dotter A., 2016, ApJS, 222, 8
Eggenberger P., Meynet G., Maeder A., Hirschi R., Charbonnel C., Talon S., Ekström S., 2008, Ap&SS, 316, 43
Eggenberger P. et al., 2021, A&A, 652, A137
Ekström S. et al., 2012, A&A, 537, A146
Eldridge J. J., Vink J. S., 2006, A&A, 452, 295
Farmer R., Fields C. E., Petermann I., Dessart L., Cantiello M., Paxton B., Timmes F. X., 2016, ApJS, 227, 22
Farrell E., Groh J. H., Hirschi R., Murphy L., Kaiser E., Ekström S., Georgy C., Meynet G., 2021, MNRAS, 502, L40
Georgy C. et al., 2013, A&A, 558, A103
Georgy C., Granada A., Ekström S., Meynet G., Anderson R. I., Wyttenbach A., Eggenberger P., Maeder A., 2014, A&A, 566, A21
Gräfener G., Hamann W. R., 2008, A&A, 482, 945
Gravity Collaboration, 2019, A&A, 625, L10
Groh J. H. et al., 2019, A&A, 627, A24
Hidalgo S. L. et al., 2018, ApJ, 856, 125
Higgins E. R., Vink J. S., 2019, A&A, 622, A50
Higgins E. R., Sander A. A. C., Vink J. S., Hirschi R., 2021, MNRAS, 505, 4874
Hirschi R., Meynet G., Maeder A., 2004, A&A, 425, 649
Kaiser E. A., Hirschi R., Arnett W. D., Georgy C., Scott L. J. A., Cristini A., 2020, MNRAS, 496, 1967
Liermann A., Hamann W. R., Oskinova L. M., 2009, A&A, 494, 1137
Liermann A., Hamann W. R., Oskinova L. M., Todt H., Butler K., 2010, A&A, 524, A82
Liermann A., Hamann W. R., Oskinova L. M., 2012, A&A, 540, A14
Lodders K., 2003, ApJ, 591, 1220
Lohr M. E., Clark J. S., Najarro F., Patrick L. R., Crowther P. A., Evans C. J., 2018, A&A, 617, A66
Maeder A., Meynet G., 2000, A&A, 361, 159
Martinet S. et al., 2021, A&A, 648, A126
Martins F., Hillier D. J., Paumard T., Eisenhauer F., Ott T., Genzel R., 2008, A&A, 478, 219
Meynet G., Maeder A., Schaller G., Schaerer D., Charbonnel C., 1994, A&AS, 103, 97
Muijres L. E., de Koter A., Vink J. S., Krtička J., Kubát J., Langer N., 2011, A&A, 526, A32
Murphy L. J. et al., 2021, MNRAS, 501, 2745
Nagata T., Woodward C. E., Shure M., Kobayashi N., 1995, AJ, 109, 1676
Najarro F., Figer D. F., Hillier D. J., Geballe T. R., Kudritzki R. P., 2009, ApJ, 691, 1816
Najarro F., de la Fuente D., Geballe T. R., Figer D. F., 2014, in Sjouwerman L. O., Lang C. C., Ott J., eds, Proc. IAU Symp. 303, The Galactic Center: Feeding and Feedback in a Normal Galactic Nucleus. Cambridge Univ. Press, p. 252
Negueruela I., Clark J. S., Ritchie B. W., 2010, A&A, 516, A78
Nugis T., Lamers H. J. G. L. M., 2000, A&A, 360, 227
Pietrinferni A., Cassisi S., Salaris M., Castelli F., 2004, ApJ, 612, 168
Pietrinferni A., Cassisi S., Salaris M., Castelli F., 2006, ApJ, 642, 797
Pietrinferni A. et al., 2021, ApJ, 908, 102
Reimers D., 1975, Mem. Soc. R. Sci. Liege, 8, 369
Reimers D., 1977, A&A, 61, 217
Ritchie B. W., Clark J. S., Negueruela I., Langer N., 2010, A&A, 520, A48
Ritter C., Herwig F., Jones S., Pignatari M., Fryer C., Hirschi R., 2018, MNRAS, 480, 538
Rosslowe C., 2016, PhD thesis, The University of Sheffield
Schaller G., Schaerer D., Meynet G., Maeder A., 1992, A&AS, 96, 269
Schneider F. R. N. et al., 2014, ApJ, 780, 117
Scott L. J. A., Hirschi R., Georgy C., Arnett W. D., Meakin C., Kaiser E. A., Ekström S., Yusof N., 2021, MNRAS, 503, 4208
Smartt S. J., Crowther P. A., Dufton P. L., Lennon D. J., Kudritzki R. P., Herrero A., McCarthy J. K., Bresolin F., 2001, MNRAS, 325, 257
Spada F., Demarque P., Kim Y. C., Boyajian T. S., Brewer J. M., 2017, ApJ, 838, 161
Stanway E. R., Eldridge J. J., 2018, MNRAS, 479, 75
Sylvester R. J., Skinner C. J., Barlow M. J., 1998, MNRAS, 301, 1083
Trundle C., Dufton P. L., Lennon D. J., Smartt S. J., Urbaneja M. A., 2002, A&A, 395, 519
Umeda H., Yoshida T., Nagele C., Takahashi K., 2020, ApJ, 905, L21
van Loon J. T., Groenewegen M. A. T., de Koter A., Trams N. R., Waters L. B. F. M., Zijlstra A. A., Whitelock P. A., Loup C., 1999, A&A, 351, 559
Venn K. A., McCarthy J. K., Lennon D. J., Przybilla N., Kudritzki R. P., Lemke M., 2000, ApJ, 541, 610
Vink J. S., de Koter A., Lamers H. J. G. L. M., 2001, A&A, 369, 574
Vink J. S., Brott I., Gräfener G., Langer N., de Koter A., Lennon D. J., 2010, A&A, 512, L7
Vink J. S., Higgins E. R., Sander A. A. C., Sabhahit G. N., 2021, MNRAS, 504, 146
Westerlund B., 1961, PASP, 73, 51
Yusof N. et al., 2013, MNRAS, 433, 1114
Zaritsky D., Kennicutt Robert C. J., Huchra J. P., 1994, ApJ, 420, 87
Zurita A., Bresolin F., 2012, MNRAS, 427, 1463

APPENDIX A: SUMMARY TABLE OF THE MODEL PROPERTIES

Table A1 lists the key properties of the present grid of models.

Table A1. Properties of the $Z = 0.020$ stellar models at the end of the H-, He-, and C-burning phases. Columns 1 to 4 give the initial mass of the model, the initial ratio between the rotational velocity at the equator and the critical rotational velocity, the initial rotational velocity at the equator, and the time-averaged equatorial surface velocity during the MS phase, respectively. Columns 5 to 11 present properties of the stellar models at the end of the core H-burning phase: age, total mass, surface equatorial velocity, ratio of the equatorial surface velocity to the critical velocity, mass fraction of helium at the surface, ratios in mass fraction of the nitrogen to carbon abundances at the surface, and of nitrogen to oxygen at the surface, respectively. Columns 12 to 17 and 18 to 22 show properties of the models at the end of the core He- and C-burning phases, respectively. The columns labelled M, $V_{\rm eq}$, $Y_{\rm surf}$, N/C, and N/O have the same meaning as the corresponding columns for the end of the core hydrogen burning phase. The quantity $\tau_{\rm He}$ ($\tau_{\rm C}$) corresponds to the duration of the He- (C-) core burning phase.

				End of H-burning							End of He-burning						End of C-burning				
$M_{\rm ini}$	$V_{\rm ini}/V_{\rm crit}$	$V_{\rm eq}$	$\bar{V}_{\rm MS}$	$\tau_{\rm H}$	M	$V_{\rm eq}$	$V_{\rm eq}/V_{\rm crit}$	$Y_{\rm surf}$	N/C	N/O	$\tau_{\rm He}$	M	$V_{\rm eq}$	$Y_{\rm surf}$	N/C	N/O	$\tau_{\rm C}$	M	$Y_{\rm surf}$	N/C	N/O
$M_\odot$		km s^{-1}		Myr	$M_\odot$	km s^{-1}			mass fract.		Myr	$M_\odot$	km s^{-1}		mass fract.		kyr	$M_\odot$		mass fract.	
300.00	0.00	0.	0.	2.194	49.48	–	–	0.9785	65.95	94.88	0.331	22.32	–	0.2366	0.00	0.00	0.015	22.23	0.2323	0.00	0.00
300.00	0.40	419.	35.	2.286	59.16	1.	0.002	0.9775	62.06	94.90	0.319	25.34	1.	0.2355	0.00	0.00	0.013	25.24	0.2312	0.00	0.00
200.00	0.00	0.	0.	2.349	78.23	–	–	0.9205	82.92	84.84	0.297	35.76	–	0.2163	0.00	0.00	0.005	35.65	0.2125	0.00	0.00
200.00	0.40	421.	56.	2.566	73.51	<1	0.000	0.9053	82.54	83.16	0.298	34.75	5.	0.2287	0.00	0.00	0.006	34.64	0.2248	0.00	0.00
150.00	0.00	0.	0.	2.504	66.47	–	–	0.8943	86.41	81.23	0.307	31.01	–	0.2253	0.00	0.00	0.008	30.92	0.2218	0.00	0.00
150.00	0.40	408.	71.	2.838	60.76	1.	0.003	0.8873	85.22	80.22	0.316	25.89	<1	0.2349	0.00	0.00	0.011	25.79	0.2309	0.00	0.00
120.00	0.00	0.	0.	2.663	56.69	–	–	0.8460	91.24	76.78	0.326	23.49	–	0.2235	0.00	0.00	0.016	23.40	0.2179	0.00	0.00
120.00	0.40	383.	82.	3.108	52.67	2.	0.004	0.8690	87.75	77.77	0.328	22.35	<1	0.2380	0.00	0.00	0.017	22.26	0.2354	0.00	0.00
85.00	0.00	0.	0.	3.005	45.81	–	–	0.6735	108.01	67.75	0.360	16.29	–	0.2458	0.00	0.00	0.038	16.21	0.2405	0.00	0.00
85.00	0.40	364.	96.	3.628	42.72	4.	0.006	0.8153	93.00	72.18	0.356	16.73	<1	0.2536	0.00	0.00	0.038	16.64	0.2480	0.00	0.00
60.00	0.00	0.	0.	3.498	33.75	–	–	0.5567	135.85	55.75	0.413	10.86	–	0.2752	0.00	0.00	0.163	10.77	0.2681	0.00	0.00
60.00	0.40	338.	120.	4.339	34.87	4.	0.007	0.7564	81.73	42.13	0.388	12.96	24.	0.2725	0.00	0.00	0.099	12.87	0.2665	0.00	0.00
40.00	0.00	0.	0.	4.377	33.96	–	–	0.2735	0.29	0.12	0.466	11.39	–	0.2138	0.00	0.00	0.140	11.33	0.2113	0.00	0.00
40.00	0.40	302.	139.	5.562	30.60	5.	0.013	0.5351	14.61	4.67	0.424	11.72	<1	0.2752	0.00	0.00	0.129	11.63	0.2707	0.00	0.00
32.00	0.00	0.	0.	5.120	29.67	–	–	0.2735	0.29	0.12	0.544	10.93	–	0.7779	91.58	58.69	0.193	10.71	0.9805	80.98	81.54
32.00	0.40	3.	163.	6.705	26.90	7.	0.016	0.4779	7.55	2.35	0.504	9.88	5.	0.2633	0.00	0.00	0.228	9.80	0.2551	0.00	0.00
25.00	0.00	0.	0.	6.228	23.98	–	–	0.2735	0.29	0.12	0.702	8.27	–	0.5438	166.45	6.28	0.483	8.04	0.9804	63.69	73.03
25.00	0.40	3.	192.	8.057	23.12	4.	0.011	0.3752	3.67	1.03	0.598	9.24	<1	0.9582	4.31	16.11	0.292	9.08	0.9563	2.25	12.86
20.00	0.00	0.	0.	7.595	19.60	–	–	0.2735	0.29	0.12	0.864	8.83	–	0.4950	40.42	3.00	1.342	8.45	0.5032	56.94	3.27
20.00	0.40	3.	209.	9.518	19.37	1.	0.003	0.3093	2.16	0.56	0.799	7.54	<1	0.6253	137.80	3.67	0.852	7.27	0.7613	130.19	10.91
15.00	0.00	0.	0.	10.837	14.78	–	–	0.2735	0.29	0.12	1.369	13.18	–	0.3265	2.30	0.58	4.868	13.09	0.3505	3.05	0.73
15.00	0.40	255.	194.	13.545	14.64	140.	0.343	0.2970	2.08	0.50	1.304	10.97	<1	0.3838	5.65	0.99	2.075	10.83	0.4013	6.36	1.08
12.00	0.00	0.	0.	15.151	11.93	–	–	0.2735	0.29	0.12	1.994	11.61	–	0.3120	1.83	0.49	10.318	11.56	0.3122	1.98	0.51
12.00	0.40	261.	193.	18.556	11.89	182.	0.452	0.2850	1.54	0.39	1.965	10.45	1.	0.3413	4.72	0.79	4.862	10.36	0.3553	5.26	0.85
9.00	0.00	0.	0.	26.110	8.99	–	–	0.2735	0.29	0.12	3.486	8.84	–	0.2935	1.58	0.42					
9.00	0.40	2.	182.	31.679	8.99	2.	0.005	0.2791	1.03	0.30	3.413	8.79	1.	0.3403	4.77	0.78					
7.00	0.00	0.	0.	42.215	7.00	–	–	0.2735	0.29	0.12	7.103	6.93	–	0.2908	1.52	0.40					
7.00	0.40	230.	175.	52.260	7.00	186.	0.501	0.2764	0.74	0.24	6.949	6.90	2.	0.3315	4.07	0.72					
5.00	0.00	0.	0.	93.975	5.00	–	–	0.2735	0.29	0.12	18.718	4.97	–	0.2902	1.46	0.39					
5.00	0.40	217.	162.	114.744	5.00	165.	0.488	0.2747	0.51	0.18	17.289	4.95	3.	0.3279	3.35	0.66					
4.00	0.00	0.	0.	165.064	4.00	–	–	0.2735	0.29	0.12	44.431	3.98	–	0.2930	1.47	0.39					
4.00	0.40	189.	153.	201.563	4.00	147.	0.473	0.2743	0.43	0.16	39.392	3.97	4.	0.3286	3.02	0.63					
3.00	0.00	0.	0.	354.769	3.00	–	–	0.2735	0.29	0.12	135.869	2.99	–	0.2947	1.45	0.38					
3.00	0.40	193.	142.	441.187	3.00	131.	0.460	0.2740	0.38	0.14	115.809	2.98	5.	0.3308	2.79	0.60					
2.50	0.00	0.	0.	589.831	2.50	–	–	0.2735	0.29	0.12	241.474	2.49	–	0.2920	1.36	0.35					
2.50	0.40	187.	136.	742.734	2.50	122.	0.450	0.2739	0.36	0.14	190.089	2.49	5.	0.3290	2.60	0.55					

Table A1 – *continued*

				End of H-burning							End of He-burning						End of C-burning				
$M_{\rm ini}$	$V_{\rm ini}/V_{\rm crit}$	$V_{\rm eq}$	$\bar{V}_{\rm MS}$	$\tau_{\rm H}$	M	$V_{\rm eq}$	$V_{\rm eq}/V_{\rm crit}$	$Y_{\rm surf}$	N/C	N/O	$\tau_{\rm He}$	M	$V_{\rm eq}$	$Y_{\rm surf}$	N/C	N/O	$\tau_{\rm C}$	M	$Y_{\rm surf}$	N/C	N/O
$M_\odot$		km s^{-1}		Myr	$M_\odot$	km s^{-1}			mass fract.		Myr	$M_\odot$	km s^{-1}		mass fract.		kyr	$M_\odot$		mass fract.	
2.00	0.00	0.	0.	1119.481	2.00	–	–	0.2735	0.29	0.12											
2.00	0.40	185.	133.	1436.772	2.00	118.	0.456	0.2740	0.34	0.13											
1.70	0.00	0.	0.	1826.804	1.70	–	–	0.2735	0.29	0.12											
1.70	0.40	150.	127.	2358.293	1.70	109.	0.422	0.2741	0.33	0.13											
1.50	0.00	0.	0.	2543.919	1.50	–	–	0.2735	0.29	0.12											
1.50	0.40	150.	10.	3024.281	1.50	9.	0.000	0.2747	0.36	0.13											
1.35	0.00	0.	0.	3743.685	1.35	–	–	0.2735	0.29	0.12											
1.35	0.40	28.	7.	4122.357	1.35	6.	0.000	0.2744	0.31	0.12											
1.25	0.00	0.	0.	5025.342	1.25	–	–	0.2285	0.29	0.11											
1.25	0.40	26.	5.	5343.693	1.25	4.	0.000	0.2623	0.30	0.12											
1.10	0.00	0.	0.	6238.572	1.10	–	–	0.2207	0.29	0.11											
1.10	0.40	50.	3.	6339.092	1.10	3.	0.000	0.2581	0.29	0.12											
1.00	0.00	0.	0.	9677.035	1.00	–	–	0.2202	0.29	0.11											
1.00	0.40	50.	2.	9895.752	1.00	2.	0.000	0.2541	0.29	0.11											
0.90	0.00	0.	0.	15196.086	0.90	–	–	0.2129	0.29	0.11											
0.90	0.40	12.	2.	15600.981	0.90	1.	0.000	0.2481	0.29	0.11											
0.80	0.00	0.	0.	24110.325	0.80	–	–	0.2011	0.29	0.11											
0.80	0.40	6.	1.	24858.578	0.80	1.	0.000	0.2391	0.29	0.11											

This paper has been typeset from a TEX/LATEX file prepared by the author.